

Optimizing the interaction geometry of inverse Compton scattering x-ray sources

C.W. Sweers* and O.J. Luiten

*Department of Applied Physics, Eindhoven University of Technology,
P.O. Box 513, 5600 MB Eindhoven, The Netherlands*

(Dated: February 6, 2026)

Inverse Compton scattering (ICS) is a promising method for generating coherent and tunable x-rays in a compact setup. In this paper, we present a theoretical framework describing the output of an ICS x-ray source for arbitrary interaction angles between pulsed electron and laser beams. This allows for analytic optimization of the x-ray beam properties by varying the parameters defining the geometry. In general, different x-ray applications require optimization of different x-ray beam properties, such as energy spread for x-ray spectroscopy and angular spread for x-ray scattering measurements. In this paper, we restrict ourselves to optimization of the x-ray brilliance, which is a comprehensive figure of merit for x-ray beam quality. We investigate two specific ICS interaction geometries in particular: head-on scattering of a laser beam off an electron beam; and scattering of a laser beam off an electron beam in a co-propagating geometry, interacting under a grazing angle. For head-on scattering we show that a tightly focused, cylindrically symmetric laser pulse, which balances laser intensity and interaction time, optimizes the x-ray brilliance. For a co-propagating, grazing angle geometry, an elliptical focus of the laser pulse is required to mitigate the effect of a reduced interaction time. We find that the latter geometry is especially useful for soft x-ray generation.

I. INTRODUCTION

Coherent and tunable x-ray sources have become an indispensable tool in many fields of research, such as materials science [1], life sciences [2], and advanced medical diagnostics [3]. This demand is primarily served by large facilities such as synchrotrons and free electron lasers [4]. However, due to the limited availability of these large facilities, their usage comes with many logistical challenges. Therefore, there is a growing need for coherent and tunable x-ray sources at the scale of the university lab.

Inverse Compton scattering (ICS), a phenomenon in which a highly energetic electron collides with a photon in such a way that the electron loses energy and the photon gains energy, forms the basis of a promising method to generate x-rays at the lab scale. Several ICS based x-ray sources are currently operational [5–11] and new designs have been proposed [12–15]. Imaging techniques that require energy tunability and coherence, such as K-edge subtraction imaging [16] and phase contrast imaging [17], have been demonstrated with an ICS based x-ray source and the use of lensless techniques such as ptychography has been proposed [18].

While the fundamental theory of ICS has been described in great detail [19–21], a closed form analytical treatment, that takes into account both the three dimensional distribution of the pulsed electron and laser beams and arbitrary interaction angles, is lacking. Optimization tasks are therefore left to simulations, which can be time consuming and do not provide a

thorough physical understanding of the limitations.

The goal of this paper is to provide an analytical closed form theoretical framework to optimize x-ray generation by ICS. Different applications require optimization of different x-ray beam properties. In this paper we choose to optimize the x-ray brilliance, which is a comprehensive figure of merit that take into account x-ray flux, transverse coherence and energy spread. The average x-ray brilliance is defined as [22]

$$B_x = \frac{f N_x}{\Delta A \Delta \Omega (\Delta \omega / \omega_x)}. \quad (1)$$

Here, N_x is the number of x-rays per pulse, f is the pulse repetition frequency, ΔA is the effective x-ray emission area, and $\Delta \Omega$ is the solid angle in which the x-rays are emitted. $\Delta \omega / \omega_x$ is the relative bandwidth of the x-ray beam. For details on the definition of the x-ray brilliance used in the paper, see Appendix C.

The framework is meant to provide an intuitive understanding of how the x-ray source performance scales with the parameters of the interaction geometry. Here, the term *geometry* refers not only to the interaction angle, but also to the electron and laser pulse dimensions, the electron beam energy, and the bunch charge. The framework could serve as a baseline for a Compton x-ray source design, in which, given a desired x-ray energy and performance of the electron beamline and laser system, the optimized interaction geometry can be calculated directly.

* c.w.sweers@tue.nl

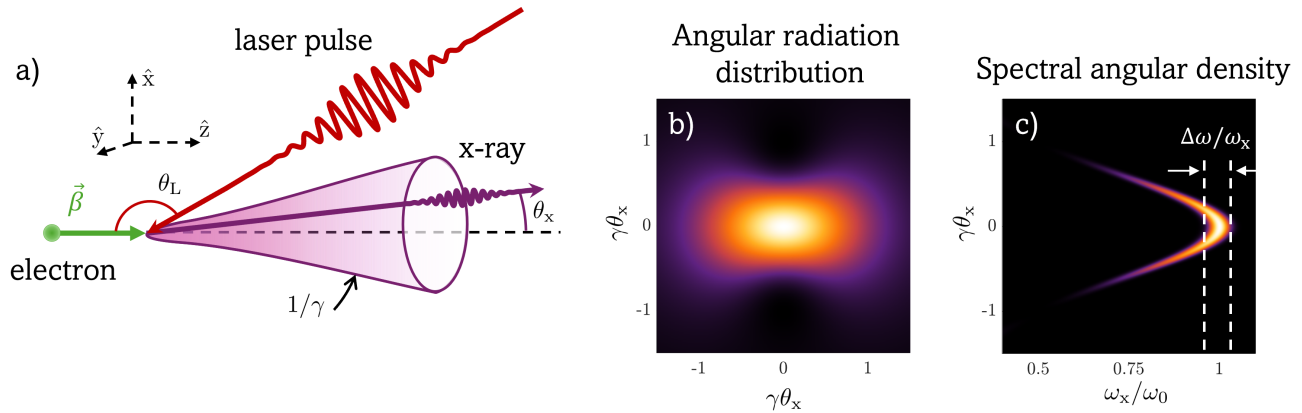


FIG. 1. a) Schematic representation of ICS. An electron (green) interacts with a laser pulse (red) under an angle θ_L , generating x-rays with emission angle θ_x . b) shows the angular radiation distribution, which becomes cylindrically symmetric for $\theta_x \ll 1/\gamma$. Here the vertical axis is in the direction of the laser polarization. c) shows the spectral angular density, with $\omega_0 = \omega_L(1 - \beta \cos \theta_L)/(1 - \beta)$ the x-ray frequency for $\theta_x = 0$

A. Basics of inverse Compton scattering

Figure 1a shows a schematic illustration of the ICS geometry. An electron (green) with velocity $\vec{v} = \beta c \hat{z}$ and normalized energy $\gamma = 1/\sqrt{1 - \beta^2}$ interacts with a laser pulse (red) under an interaction angle θ_L , w.r.t. the electron velocity. This angle is defined in such a way that $\theta_L = \pi$ corresponds to a head-on collision. During the interaction, the electron oscillates rapidly and radiates in the process (purple). Due to the relativistic nature of the electron, the radiation becomes strongly blue shifted. The shifted frequency is given by [21]

$$\omega_x = \omega_L \frac{1 - \beta \cos \theta_L}{1 - \beta \cos \theta_x} \quad (2)$$

Here, ω_x and ω_L are the angular frequencies of the generated radiation and the laser pulse, respectively, and θ_x is the angle of the outgoing radiation with respect to the electron velocity.

In the relativistic limit ($\gamma \gg 1$) and under small radiation angles ($\gamma \theta_x \ll 1$), Eq. (2) can be approximated in a convenient way. For head-on scattering ($\theta_L = \pi$) this results in the well known expression

$$\omega_x \Big|_{\theta_L=\pi} \simeq \omega_L \frac{4\gamma^2}{1 + \gamma^2 \theta_x^2}, \quad (3)$$

whereas for small interaction angles ($\theta_L \ll 1$) we find

$$\omega_x \Big|_{\theta_L \ll 1} \simeq \omega_L \frac{1 + \gamma^2 \theta_L^2}{1 + \gamma^2 \theta_x^2}. \quad (4)$$

Note that, since typically a large frequency shift is desired, preferably $\gamma \theta_L \gg 1$. These approximations clearly show that the x-ray energy can be tuned by varying either the electron energy, γ , or the interaction

angle θ_L .

Furthermore, Eqs. (3) and (4) show how the x-ray frequency depends on the angle θ_x : the highest x-ray frequency, ω_0 , is emitted along the propagation direction of the electron ($\theta_x = 0$) and the x-ray frequency gradually decreases for larger angles, as shown in Fig 1c. At $\theta_x \simeq 1/\gamma$ the x-ray frequency has become half of the on-axis frequency, ω_0 . Fig 1b shows the intensity distribution of ICS, which is concentrated in a narrow cone characterized by a half angle $\theta_x = 1/\gamma$ [23]. The distribution is slightly asymmetric for linear laser polarization, which is pointing in the vertical direction in Fig 1b. However, for $\theta_x \ll 1/\gamma$, which is required for a narrow bandwidth x-ray beam, the angular distribution of the radiation is to a good approximation uniform.

The central challenge in the development of Compton x-ray sources lies in the low efficiency of x-ray generation per electron, associated with the small Thomson cross section,

$$\sigma_T = \frac{8\pi}{3} r_e^2 \simeq 66.5 \text{ fm}^2, \quad (5)$$

where $r_e = e^2/(4\pi\epsilon_0 mc^2)$ is the classical electron radius, with e the elementary charge and m the electron mass. Obviously, for efficient generation of x-rays by Compton scattering, the density of electrons and laser photons needs to be as high as possible, requiring focused electron and laser pulses.

B. Structure of this paper

We will analyze the dependence of the x-ray generation on geometry of ICS in increasing levels of complexity,

illustrated by Fig. 2. We start in Sec. II by describing ICS in a head-on geometry using a collisional model. We first consider the collision between pencil beams, i.e. in the approximation of perfectly parallel beams (① in Fig. 2). Next, we analyze the more realistic situation of a focused laser pulse and a pencil electron beam (② in Fig. 2) and find the optimized interaction spot size and the corresponding optimized bunch charge.

In Sec. III, we analyze ICS for arbitrary interaction angles. This is the most novel part of the paper. A proper analysis of this geometry requires a treatment in a covariant framework. Again, we first analyze the situation of two pencil beams (③ in Fig. 2). Subsequently, we investigate the combination of a focused laser pulse and a pencil electron beam (④ in Fig. 2). We derive closed form analytical expressions for the laser focal spot size and the electron bunch charge, which optimize the x-ray brilliance in a grazing angle geometry. We find that a shallow co-propagating interaction angle – a *grazing angle geometry* – can be favorable compared to a head-on geometry, especially for the generation of soft x-rays.

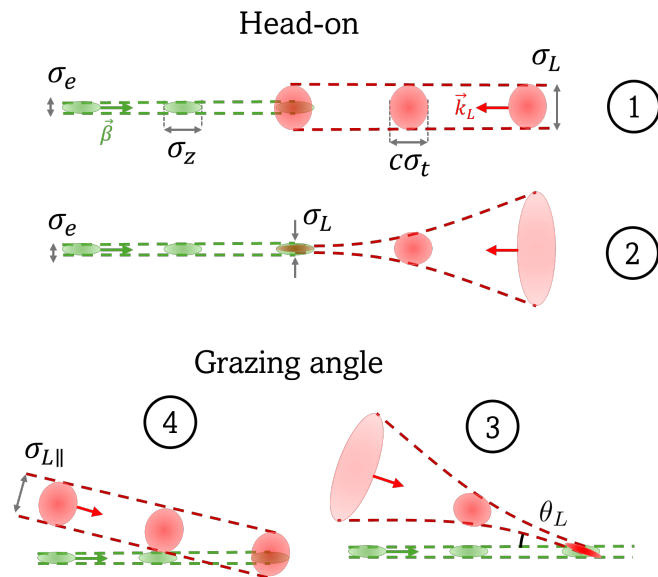


FIG. 2. Schematic illustrations of the four geometries considered in this paper. In each geometry the electron bunch (green) with velocity β and laser pulse (red) with wave vector \mathbf{k}_L are shown at three different times up until the collision. The top figures show the pencil beam ① and focused laser beam ② geometries in a head-on geometry. The bottom figures show the pencil beam ③ and focused laser beam ④ geometries in a grazing angle geometry. The relevant r.m.s. pulse dimensions are also indicated

II. HEAD-ON INVERSE COMPTON SCATTERING

In this section we describe ICS in a head-on geometry ($\theta_L = \pi$). We start with a pencil beam description and calculate the x-ray brilliance. The result from this simplified model serves as a demonstration of important scalings for ICS. Next, we consider a finite laser pulse length to find the optimal laser waist. Finally, a simple argument is used to determine the bunch charge that maximizes the x-ray brilliance.

A. Pencil beam description

We assume the pulses to be pencil beams with a Gaussian transverse photon/electron density distribution

$$\rho_{L,e} = \frac{N_{L,e}}{2\pi\sigma_{L/e}^2} \exp\left(-\frac{x^2 + y^2}{2\sigma_{L/e}^2}\right), \quad (6)$$

where the subscripts L and e refer to the laser beam and the electron beam, respectively. $N_{L/e}$ is the total number of laser photons/electrons and $\sigma_{L/e}$ is the r.m.s. transverse size. Throughout this paper, a quantity σ refers to an r.m.s. quantity (with the exception of the Thompson cross section σ_T). Note that we can neglect the z -dependence of the density distributions due to the head-on geometry and the pencil beam approximation. The total number of scattered x-rays in the collision is given by [24]

$$N_x = \sigma_T \int dt \int d\mathbf{x} \rho_L \rho_e |v_e - v_L| = \frac{\sigma_T N_L N_e}{2\pi(\sigma_e^2 + \sigma_L^2)}, \quad (7)$$

Note that Eq. (7) corresponds to the situation in which the x-rays are scattered in the complete 4π solid angle with 100% relative energy spread. If a small relative energy spread $\Delta\omega/\omega_x$ is required, the x-ray acceptance angle should be reduced to $\Theta_x = \sqrt{(\Delta\omega/\omega_x)/\gamma}$. If $\gamma\Theta_x \ll 1$, the number of x-rays in this acceptance angle is [23]

$$N_x = \frac{\sigma_T N_L N_e}{4\pi\sigma_e^2} \frac{3}{2} \gamma^2 \Theta_x^2. \quad (8)$$

Here, we have additionally assumed that the sizes of the electron and laser pulses are matched ($\sigma_L = \sigma_e$), which is close to the optimized situation and simplifies the analysis. This is an important assumption used throughout this section. Using $\Delta A \Delta \Omega = 2\pi^2 \sigma_e^2 \Theta_x^2$ and $\Delta\omega/\omega_x = \sqrt{2\pi} \sigma_\omega/\omega_x$, with σ_ω/ω_x the r.m.s. relative bandwidth, the average brilliance is given by

$$B_x = \frac{f \sigma_T N_L N_e}{\sqrt{2\pi}} \frac{3}{8\pi^3} \frac{1}{2} \frac{\gamma^2 \Theta_x^2}{\sigma_e^4 \Theta_x^2 \sigma_\omega/\omega_x}. \quad (9)$$

The energy spread of a Compton x-ray source has several contributions originating from both the laser pulse

and the electron beam properties [25]. To illustrate important scalings, we restrict ourselves in the first instance to the contribution to the energy spread due to the angular spread of the electron beam: $\sigma_\omega/\omega_x|_{\sigma_{\theta_e}} = \gamma^2\sigma_{\theta_e}^2$. If we describe the electron beam using the normalized emittance, $\epsilon_n = \gamma\beta\sigma_e\sigma_{\theta_e} \simeq \gamma\sigma_e\sigma_{\theta_e}$, Eq. (9) can be rewritten as

$$B_x = \frac{f\sigma_T N_L N_e}{\sqrt{2\pi}} \frac{3}{8\pi^3} \frac{\gamma^4 \sigma_{\theta_e}^2}{2 \epsilon_n^4}. \quad (10)$$

Equation (10) shows two important scalings: First, we find that the brilliance scales with γ^4 , which originates from the improved geometric emittance with increased electron energy. This not only results in a smaller x-ray source size, but also allows for tighter focusing of the laser pulse. In a head-on geometry, the electron energy is fixed by the desired x-ray energy for a given laser wavelength. However, if the interaction angle can be varied, this scaling can be exploited for any desired x-ray energy. This will be further explored in Sec. III.

Second, Eq. (10) shows that $B_x \propto N_e/\epsilon_n^4$. For space charge dominated electron beams, it holds that $N_e/\epsilon_n^2 = \text{constant}$. As a result we find that the x-ray brilliance increases with a lower bunch charge. This counterintuitive result is a direct consequence of the assumption that the spot size of the electron and laser beams are matched ($\sigma_L = \sigma_e$), which is an assumption that cannot hold indefinitely, as it is obviously limited by the laser beam diffraction limit. In the remainder of this section we calculate the x-ray flux and brilliance with realistic electron and laser beam descriptions, and find the optimized laser focus and the corresponding bunch charge to match the electron spot size to the laser pulse.

B. Focused laser pulse

Before the laser beam diffraction limit is reached, the Rayleigh range may become comparable to, or even smaller than, the laser pulse length, resulting in a significant reduction of the interaction time between the electron pulse and the laser pulse (see Fig. 3). This will lead to both a reduction of the number of x-ray photons produced, and an increase of the x-ray energy spread. To analyze the effect of focusing the laser beam we now consider the photon density of a TEM₀₀ pulsed Gaussian laser beam

$$\rho_L = \frac{N_L}{(2\pi)^{3/2} \sigma_L^2(z) \sigma_t} \exp\left[-\frac{x^2 + y^2}{2\sigma_L^2(z)} - \frac{(z/c + t)^2}{2\sigma_t^2}\right], \quad (11)$$

where σ_t is the laser pulse length and $\sigma_L(z) = \sigma_L(0)\sqrt{1 + (z/z_R)^2}$ with $z_R = 2k_L\sigma_L^2$ the Rayleigh length. Throughout this paper we assume perfect laser

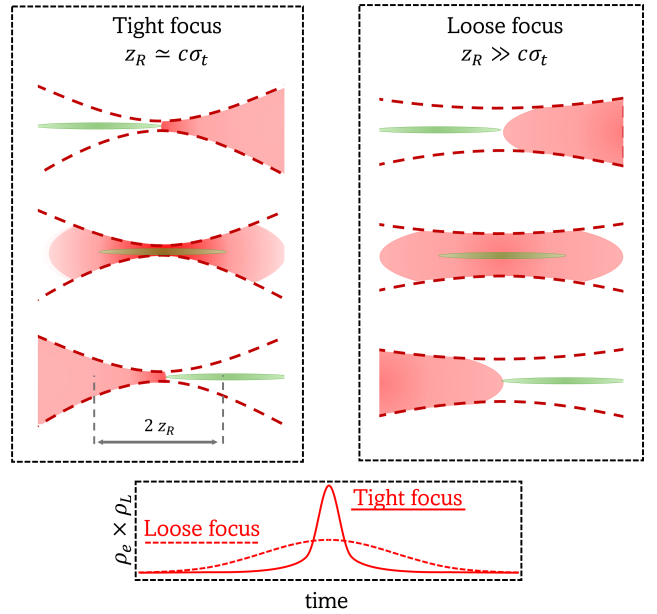


FIG. 3. Illustration showing how focusing the laser beam results in a reduction of the Rayleigh length, which affects the interaction time. The bottom graph shows the product of the electron pulse density and laser pulse photon density as a function of time for a tight focus and a loose focus.

beams ($M^2 = 1$). For non-perfect laser beams the analysis still holds if the expressions for the Rayleigh length and the angular spread are adjusted accordingly. For now, we assume the electron beam to be described by a pencil beam. Substituting (11) into the central term of Eq. (7) and subsequently performing the integration over time results in

$$N_x = \frac{\sigma_T N_L N_e}{4\pi\sigma_e^2} \frac{3}{2} \gamma^2 \Theta_x^2 \sqrt{\pi} u \operatorname{erfcx}(u). \quad (12)$$

Here, $\operatorname{erfcx}(x) = \exp(x^2)\operatorname{erfc}(x)$ is the scaled complementary error function [26], and $u = 2z_R/c\sigma_t$. The term $\sqrt{\pi} u \operatorname{erfcx}(u)$ describes how the effective interaction time is reduced due to laser beam divergence [19]. If we assume $\epsilon_n/\gamma \ll \lambda_L/4\pi$, a very reasonable assumption in practice, then also the divergence and finite longitudinal size σ_z of the electron beam can be taken into account using $u = 2z_R/\sqrt{(c^2\sigma_t^2 + \sigma_z^2)}$.

To calculate the brilliance, we must now take into account the x-ray energy spread, to which both the laser beam properties and the electron beam properties contribute. Here we consider only the three contributions of the laser beam. First, we take into account the Fourier limited bandwidth $\sigma_\omega/\omega_x|_{\omega_L} = 1/(2\omega_L\sigma_t)$, which is broadened due to the shorter interaction time:

$$\sigma_\omega/\omega_x|_{\omega_L} = 1/[2\omega_L\sigma_t\sqrt{\pi} u \operatorname{erfcx}(u)]. \quad (13)$$

Second, the angular spread of a focused laser pulse gives rise to a spread in the interaction angle $\sigma_{\theta L} = 1/(2k_L\sigma_L)$, resulting in additional x-ray broadening. By expanding Eq. (2) around $\theta_L = \pi$ we find $\sigma_\omega/\omega_x|_{\sigma_{\theta L}} = 1/(2k_L\sigma_L)^2$ [25], which can be expressed in terms of u as

$$\sigma_\omega/\omega_x|_{\sigma_{\theta L}} = \frac{1}{\omega_L\sigma_t u} \quad (14)$$

Finally, at high field intensities the x-ray energy spread is increased due to nonlinear broadening [27], characterized by the normalized vector potential amplitude $A_0 = eE_0/(mc\omega_L)$. The corresponding x-ray energy spread is given by [25]

$$\sigma_\omega/\omega_x|_{A_0} \simeq \frac{1}{6}A_0^2 = \frac{\chi}{\omega_L\sigma_t u}. \quad (15)$$

In the right hand side term we have expressed the nonlinear broadening in terms of the laser pulse dimensions. Here, $\chi = 4\sigma_T N_L/(3\sqrt{\pi}\alpha\lambda_L c\sigma_t)$ relates the laser peak power to the normalized vector potential and α is the fine structure constant. χ is only dependent on the laser pulse energy and duration, and *not* the focal spot size. The nonlinear broadening can become the significant contribution to the x-ray energy spread if the laser is tightly focused. We note that the nonlinear broadening can be circumvented using appropriate laser pulse chirping [28], which would effectively bring $\chi \rightarrow 0$.

The three energy spread contributions associated with the laser beam properties can be combined, resulting in the following expression for the x-ray brilliance

$$B_x = \frac{3f\sigma_T N_L N_e \gamma^2 \omega_L \sigma_t}{\sqrt{2\pi} 8\pi^3 \sigma_e^4} \frac{\pi u^2 \operatorname{erfcx}(u)^2}{\sqrt{1 + 4\pi(1 + \chi^2)\operatorname{erfcx}(u)^2}}. \quad (16)$$

To optimize brilliance, we note that for space charge limited electron beams $\epsilon_n = \eta\sqrt{eN_e}$ [29], where η is a property of the injector that describes the electron beam emittance at given bunch charge. Therefore $N_e/\sigma_e^2 = \text{constant}$. Since $u \propto \sigma_L^2 = \sigma_e^2$, the function $g(u) = \pi u \operatorname{erfcx}(u)^2/\sqrt{1 + 4\pi(1 + \chi^2)\operatorname{erfcx}(u)^2}$ must be maximized, resulting in the optimized value for σ_e

$$\sigma_e^{\text{opt}} = \sqrt{u_{\max}\lambda_L c\sigma_t/8\pi} \quad (17)$$

where u_{\max} is the value of u that maximizes $g(u)$ and thus the x-ray brilliance. To take into account the length of the electron pulse σ_z , the substitution $\sigma_t \rightarrow \sigma_t\sqrt{1 + (\sigma_z/c\sigma_t)^2}$ should be used in Eq. (17). If bandwidth contributions from the electron beam are taken into account, additional terms should be added to the square root of $g(u)$. Then, a larger energy spread is allowed from the laser pulse, resulting in a lower value of u_{\max} .

In Fig. 4 the function $g(u)$ is plotted for $\chi = 0$ (green curve) and $\chi = 5$ (blue curve), respectively. The

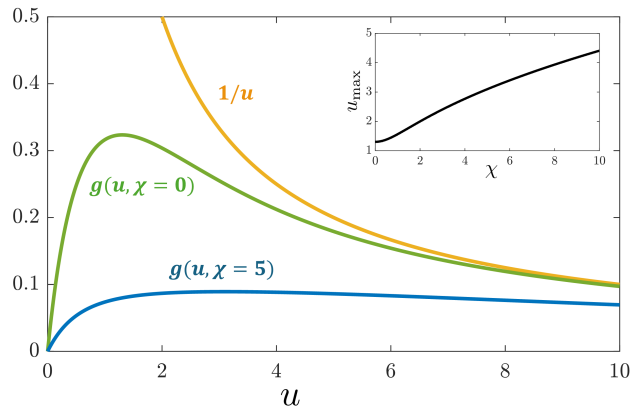


FIG. 4. Plots of the function $g(u)$ for $\chi = 0$ (green curve) and $\chi = 5$ (blue curve). The inset shows a plot of u_{\max} as a function of χ . For comparison the function $1/u$ (yellow curve) is plotted as well, which gives the brilliance scaling of the pencil beam limit.

function $1/u$ (yellow curve) is plotted as well, which gives the brilliance scaling in the pencil beam limit. The inset shows a plot of u_{\max} as a function of χ .

This analysis has been performed under the assumption that the electron and laser spot sizes are matched, i.e., $\sigma_e = \sigma_L$. For a fixed energy, the electron spot size is determined by the beam divergence $\sigma_{\theta e}$ and the normalized emittance ϵ_n . For relativistic beams $\sigma_{\theta e}$ is typically limited in practice to a few milliradians. We choose a fixed electron beam divergence of 1 mrad and optimize the normalized emittance such that $\sigma_e = \sigma_L$. To arrive at an expression for the optimized bunch charge we use the fact that $\epsilon_n = \eta\sqrt{eN_e} = \gamma\sigma_e\sigma_{\theta e}$, combined with Eq. (17). This results in

$$eN_e^{\text{opt}} = u_{\max}\gamma^2\sigma_{\theta e}^2 \frac{\lambda_L c\sigma_t}{8\pi\eta^2}, \quad (18)$$

which is the bunch charge that allows for the optimized electron spot size σ_e^{opt} .

C. Optimized head-on geometry

As an example, we calculate the brilliance of an ICS source generating 10 keV x-rays in a head-on geometry. The electron bunches are generated from a C-band photoinjector [30, 31] that is able to create 200 pC electron bunches at $\epsilon_n = 200$ nmrad ($\eta = 14$ nmrad/ $\sqrt{\text{pC}}$) and a relative energy spread of 0.2%. The electrons are accelerated to $\gamma = 46$ to generate 10 keV x-rays with a 5 mJ, 100 fs, 1030 nm interaction laser pulse ($\chi = 5.6$) [32]. In this example, we take the electron divergence angle to be $\sigma_\theta = 1$ mrad, and the electron pulse length and the laser pulse length are equal. Both

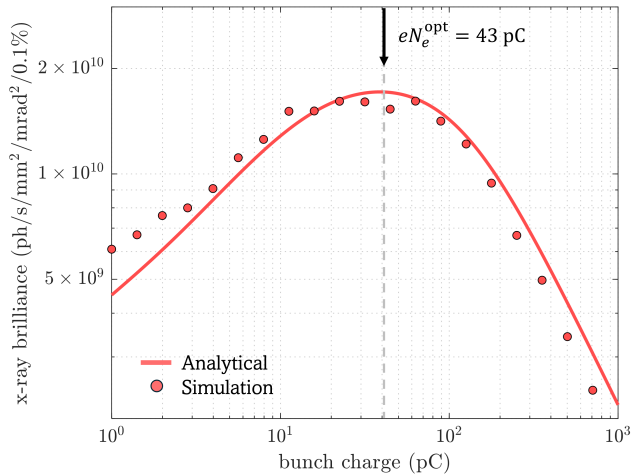


FIG. 5. X-ray brilliance for 10 keV x-ray generation in a head-on geometry with matched electron and laser spot sizes, as a function of bunch charge. The analytical result of Eq. (16) (solid curve) agrees well with simulation results (dots). The arrow marks the optimized bunch charge given by Eq. (18)

the photoinjector and the laser operate at $f = 1$ kHz.

Figure 5 shows the x-ray brilliance as a function of bunch charge. Here the bunch charge determines $\sigma_e = \eta\sqrt{eN_e}/(\gamma\sigma_{\theta_e})$ and the size of the laser is matched to the electron beam, $\sigma_L = \sigma_e$. This results in a bunch charge where σ_L and σ_e are optimized. The energy spread contributions due to the electron beam properties have also been included. The continuous curve is calculated using Eq. (16), and the dots are the result of particle tracking simulations (General Particle Tracer [33]) and subsequent numerical calculation of the Liénard-Wiechert potentials [34]. From Eqs. (17) and (18) it then follows that $\sigma_e^{\text{opt}} = 2.4 \mu\text{m}$ and the corresponding optimized bunch charge $eN_e^{\text{opt}} = 43 \text{ pC}$.

At the relatively low bunch charge of 43 pC, the x-ray brilliance is 10 times higher than at 1 nC. Additionally, the total number of scattered x-rays is only 4% lower at 43 pC than at 1 nC. Remarkably, due to the optimization of the laser focus and bunch charge, ICS is significantly more efficient at a bunch charge which is ~ 20 times lower.

III. INVERSE COMPTON SCATTERING FOR ARBITRARY INTERACTION ANGLES

In a head-on ICS geometry, the generated x-ray energy increases with the electron energy. For a given laser wavelength, the desired x-ray energy therefore determines the electron energy. At the same time, the x-ray brilliance increases with electron energy, implying that, using ICS, the generation of hard x-rays is more

favorable than the generation of soft x-rays. However, if instead of the electron energy, the interaction angle is varied to achieve the required x-ray energy, an additional degree of freedom is introduced, which allows further exploitation of the favorable scaling of the brilliance with the electron beam energy. This will be explored in some detail in this section. We will find that a grazing angle geometry (see Fig. 1) can be particularly useful for the generation of high-brilliance soft x-rays.

We will now use the framework of covariant electrodynamics, with the metric $g^{\mu\nu} = \text{diag}(1, -1, -1, -1)$, to describe the interaction of a relativistic electron bunch with a laser pulse under an arbitrary interaction angle. We start, in Sec. III A, by considering a single electron interacting with a Gaussian pencil beam. Next, in Sec. III B, we investigate the effects of focusing the laser beam, and in Sec. III C, an electron bunch of finite dimensions instead of a single electron. In Sec. III D the x-ray brilliance is optimized for $\theta_L \ll 1$. Finally, in Sec. III E, the optimized performances of ICS in a grazing angle geometry and in a head-on geometry are compared.

A. Single electron with a pencil laser beam

In the regime where electron recoil can be ignored, *i.e.*, $\hbar\omega_x/\gamma mc^2 \ll 1$, a single electron with 4-trajectory $x^\mu(\tau)$ and 4-velocity $u^\mu(\tau)$ radiates, according to the Liénard-Wiechert potentials, with a spectral angular density [19]

$$\mathcal{S}(\omega, \theta_x) = \frac{\partial^2 N_x}{\partial\omega\partial\Omega} = \frac{\alpha\omega_x}{4\pi^2} \left| \int u^\mu \exp(ik'_x{}^\nu x_\nu) d\tau \right|^2 \quad (19)$$

Here $k'_x{}^\mu = k_x(1, \mathbf{n}_x)$ is the four-wave vector of the scattered x-rays with \mathbf{n}_x the propagation direction. Furthermore, $x^\mu = (ct, \mathbf{x})$ is the electron four-position, $u^\mu = \gamma(1, \boldsymbol{\beta})$ its normalized four-velocity, and $\tau = t/\gamma$ is the proper time.

The x-ray brilliance is closely related to the spectral angular density. Using the fact that, obviously, $\sigma_e \ll \sigma_L$ for a single electron,

$$B_x \simeq \frac{fN_e}{2\pi\sigma_e^2} \omega_0 \mathcal{S}(\omega_0, 0). \quad (20)$$

The dimensionless quantity $\omega_0 \mathcal{S}(\omega_0, 0)$ is the peak normalized spectral angular density, which is maximized for $\theta_x = 0$ and therefore $\omega = \omega_0 = 2\gamma^2\omega_L(1 - \beta \cos\theta_L)$. In this section we will analyze how $\omega_0 \mathcal{S}(\omega_0, 0)$ depends on the interaction geometry of ICS. Specifically, how it depends on the laser pulse dimensions, interaction angle and electron energy.

The integral in Eq. (19) is solved by considering a single electron that experiences the normalized vector potential, with amplitude $A(\tau)$, due the laser pulse. We assume that this normalized vector potential is Gaussian,

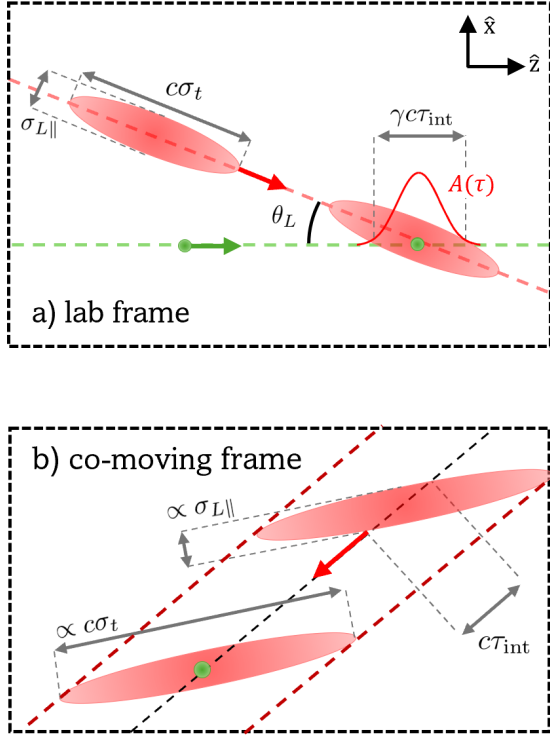


FIG. 6. Illustrations on how the proper interaction time τ_{int} is reduced by $\sigma_{L\parallel}$ in both the lab frame (a) and the co-moving frame (b).

i.e. $A(\tau) = A_0 \exp(-\tau^2/2\tau_{\text{int}}^2)$. Here, τ_{int} is the proper interaction time of the electron with the laser pulse. Note that τ_{int} is *not* equal to the length of the laser pulse. The manner in which τ_{int} depends on the parameters of the laser pulse is discussed later. A_0 can be written in terms of the laser pulse dimensions

$$A_0^2 = \frac{3\sigma_T N_L}{2\alpha\pi^{3/2}} \frac{1}{\sigma_{L\parallel}\sigma_{L\perp}\omega_L\sigma_t}. \quad (21)$$

Because of the asymmetry in the interaction geometry, we also have to consider an asymmetric laser pulse focus with two transverse sizes, $\sigma_{L\parallel}$ and $\sigma_{L\perp}$. Here, the subscripts \parallel and \perp refer to the directions parallel and perpendicular to the x-z plane, respectively.

When nonlinear effects can be neglected, *i.e.* $A_0 \ll 1$, the peak normalized spectral angular density due to a single electron is given by the concise expression

$$\omega_0 \mathcal{S}(\omega_0, 0) = \frac{1}{8\pi} \alpha A_0^2 \omega_x^2 \tau_{\text{int}}^2 \quad (22)$$

For details, we refer to Appendix A. In this expression all dependencies on the interaction geometry are implicit in A_0 and τ_{int} . In a head-on geometry ($\theta_L = \pi$) the proper interaction time $\tau_{\text{int}} = \sqrt{2}\sigma_t/[\gamma(1+\beta)]$, while for $\theta_L = 0$, $\tau_{\text{int}} = \sqrt{2}\sigma_t/[\gamma(1-\beta)]$.

For intermediate interaction angles, $0 < \theta_L < \pi$, τ_{int} depends on $\sigma_{L\parallel}$. This is illustrated in Fig. 6a, which shows the electron (green) crossing the laser pulse (red) under an angle θ_L . The vector potential amplitude, as experienced by the electron, is illustrated by the red solid curve. Due to the less than infinite value of $\sigma_{L\parallel}$, the time that the electron and the laser pulse overlap is reduced; for $\sigma_{L\parallel} = 0$, the overlap time would be reduced to zero. In the co-moving frame (Fig. 6b) this can be understood as the electron experiencing a tilted laser pulse front. Therefore, the experienced vector potential amplitude becomes a function of both the pulse length, σ_t and transverse size $\sigma_{L\parallel}$.

The reduction in the interaction time can be quantified by a dimensionless parameter $\zeta \in [0, 1]$, defined as the ratio between the proper interaction time and the Lorentz transformed laser pulse length:

$$\zeta \equiv \left[1 + \left(\frac{\beta \sin \theta_L}{1 - \beta \cos \theta_L} \frac{c\sigma_t}{\sigma_{L\parallel}} \right)^2 \right]^{-1/2}. \quad (23)$$

Consequently, the proper interaction time is given by

$$\tau_{\text{int}} = \frac{\sqrt{2}\sigma_t\zeta}{\gamma(1-\beta\cos\theta_L)} \simeq 2\sqrt{2}\gamma\sigma_t\zeta\omega_L/\omega_x, \quad (24)$$

where we used $\gamma \gg 1$.

Figure 7 shows how ζ depends on the interaction angle θ_L for various aspect ratios $\sigma_{L\parallel}/c\sigma_t$. In a head-on geometry ($\theta_L = \pi$), it is obvious that $\zeta = 1$. For $\theta_L = 0$ the laser pulse propagates in the same direction as the electron beam and again $\zeta = 1$. However, for $0 < \theta_L < \pi$, the interaction time strongly depends on θ_L . The effect on ζ is most extreme at small interaction angles, a *grazing angle geometry*, with ζ going through a minimum at $\theta_L = \cos^{-1}(\beta) \simeq 1/\gamma$.

The effect of the reduced overlap can be overcome by either applying a pulse front tilt to the laser that corrects for the tilted front in the co-moving frame [35–37]; or by utilizing a line focused laser pulse, where $\sigma_{L\parallel} \gg \sigma_{L\perp}$. In this work we will analyze the second solution.

As an example, a 100 fs laser pulse focused to $\sigma_L = 2.4 \mu\text{m}$ interacting under $\theta_L = 10^\circ$ at $\gamma = 50$, lowers the interaction time by a factor $\zeta = 0.007$. As a result, the brilliance is reduced by more than four orders of magnitude. Utilizing a line focus, with aspect ratio $\sigma_{L\parallel}/\sigma_{L\perp} = 100$, we find that $\zeta = 0.58$. While the laser intensity is now lower (by a factor of 100), the x-ray brilliance is almost two orders of magnitude higher than if a tight symmetrical focus was applied.

The blue curve in Fig. 7 shows that also for small deviations from $\theta_L = \pi$ the interaction time can become

significantly reduced when utilizing a tight laser focus. This suggests that in a head-on geometry, it may pay off to approach $\theta_L = \pi$ as closely as possible, for instance by using parabolic mirrors with through holes [38].

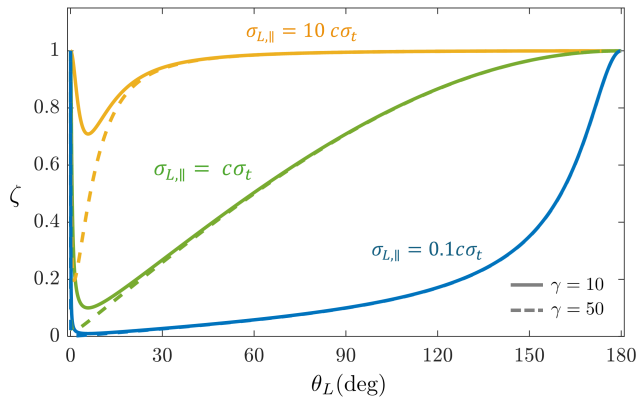


FIG. 7. Reduction ζ of the overlap time as a function of the interaction angle θ_L for three values of the ratio $\sigma_{L,||}/c\sigma_t$ (blue, green, and yellow curves) for $\gamma = 10$ (solid curves) and for $\gamma = 50$ (dashed curves).

In Sec. III D we will find expressions for the optimized laser pulse dimensions. To find these, however, we first need to describe the effect of using a focused laser beam at arbitrary interaction angles.

B. Single electron with a focused laser beam

Similar to Sec. II B, we have found that a tight laser focus is required to optimize the ICS interaction. Therefore we need to consider the effect of a focused laser pulse. In contrast to Sec. II B, we now only have a tight focus in the y-direction. Additionally, since the interaction angle is no longer parallel to the electron velocity, the electron no longer traverses the complete longitudinal profile of the laser pulse. The effect of a focused laser pulse for grazing angle ICS is analyzed using the substitution $A(\tau) \rightarrow A(\tau)/\sqrt{1 + \tau^2/\tau_R^2}$, similar to the method presented in [39]. Here we have introduced a proper Rayleigh time,

$$\tau_R = \frac{4k_L\sigma_{L,\perp}^2}{\gamma\beta c \cos\theta_L} \left(1 + \frac{\sigma_{L,\perp}^4}{\sigma_{L,\parallel}^4}\right)^{-1/2}, \quad (25)$$

which describes the proper time that the electron spends within the Rayleigh range of the laser pulse. When this time becomes small compared to the interaction time the number of scattered photons is reduced and the x-ray bandwidth is increased. The effect can be taken into account by the substitution

$$\tau_{\text{int}} \rightarrow \tau_{\text{int}}\psi \mathcal{K}_0(\psi^2/4) \quad (26)$$

with $\mathcal{K}_0(x) = \exp(x)K_0(x)/\sqrt{2\pi}$ the exponentially scaled Bessel function of second kind and order zero, and $\psi = \tau_R/\tau_{\text{int}}$. The role of ψ is also similar to that of u from Sec. II B. However, ψ describes the effect of laser pulse divergence on the interaction time at any interaction angle. In a head-on geometry, $\psi = u$. This result is very similar of the result from Eq. (12) since $\sqrt{\pi} \operatorname{erfcx}(x) \simeq \mathcal{K}_0(x^2/4)$.

In a line focus geometry, where $\sigma_{L,\perp} \ll \sigma_{L,\parallel}$, ψ can be rewritten as

$$\psi \simeq \frac{1 - \beta \cos\theta_L}{\beta \cos\theta_L} \frac{2k_L^2\sigma_{L,\perp}^2}{\omega_L\sigma_t\zeta} \quad (27)$$

When the interaction angle $\theta_L \ll 1$, $\psi \propto 1/\gamma^2$. This is a consequence of the long interaction length, $\gamma\beta c\tau_{\text{int}}$, in a grazing angle geometry with a line focused laser pulse. Therefore, $\sigma_{L,\perp}$ needs to be larger, compared to the head-on case, to ensure that the Rayleigh length in the perpendicular direction does not reduce the interaction time. In Sec. III D we will find an expression for $\sigma_{L,\perp}$ that optimizes the x-ray brilliance.

In addition to a reduced interaction time, the angular spread of the focused laser pulse also induces an additional x-ray bandwidth that is not yet included in Eq. (26). The angular spread introduces a spread in the Doppler shift. This can be quantified by an expansion of Eq. (2) around θ_L , resulting in

$$\sigma_\omega/\omega_x|_{\sigma_{\theta L}} = \frac{\beta \cos\theta_L}{1 - \beta \cos\theta_L} (\sigma_{\theta L,\parallel}^2 + \sigma_{\theta L,\perp}^2). \quad (28)$$

Here $\sigma_{\theta L,\parallel}$ and $\sigma_{\theta L,\perp}$ are angular spreads of the laser pulse parallel and perpendicular to the x-z plane respectively. We note that one would also expect a term in Eq. (28) that is first order in $\sigma_{\theta L,\parallel}$, however this term is already taken into account by ζ . For a line focused laser pulse, Eq. (28) can be rewritten as

$$\sigma_\omega/\omega_x|_{\sigma_{\theta L}} = 1/(\omega_L\sigma_t\zeta\psi). \quad (29)$$

Eq. (22) only takes into account the Fourier limited bandwidth

$$\sigma_\omega/\omega_x|_{\omega_L} = 1/[2\omega_L\sigma_t\zeta\psi \mathcal{K}_0(\psi^2/4)]. \quad (30)$$

By combining the above two expressions, we find the following expression for the peak normalized spectral angular density

$$\omega_x \mathcal{S}(\omega_x, 0) = \frac{1}{\pi} \alpha A_0^2 \gamma^2 \omega_L^2 \sigma_t^2 \zeta^2 \frac{\psi^2 \mathcal{K}_0(\psi^2/4)^2}{\sqrt{1 + 4\mathcal{K}_0(\psi^2/4)^2}} \quad (31)$$

Other bandwidth contributions can be included in the same method as discussed in Sec. II B. For the laser parameters under consideration, the bandwidth due to non-linear broadening can be neglected due to the use of the line focus.

C. Focused electron and laser beams

Up to now, we have only considered the interaction of a single electron with the laser pulse. We will now also take into account the finite electron bunch size and angular spread by means of correction terms.

The finite size of the electron beam can be taken into account by considering an electron with offset (x, y, z) at $t = 0$. This electron will probe a lower intensity of the laser pulse and therefore radiate fewer x-rays. Note that the x-ray bandwidth remains unaffected. For an electron bunch with initial density distribution

$$\rho_e(t=0) = \frac{N_e}{(2\pi)^{3/2}\sigma_e^2\sigma_z} \exp\left(-\frac{x^2+y^2}{2\sigma_e^2} - \frac{z^2}{2\sigma_z^2}\right), \quad (32)$$

we find that the total number of scattered x-rays is reduced by a factor $1 + \Sigma$, where

$$\begin{aligned} \Sigma = & \frac{\sigma_e^2(1 - \beta \cos \theta_L - \sin^2 \theta_L)^2/\beta^2 + \sigma_z^2 \sin^2 \theta_L}{4\sigma_{L\parallel}^2(1 - \beta \cos \theta_L)^2 + 4\beta^2 c^2 \sigma_t^2 \sin^2 \theta_L} \\ & + \frac{\sigma_e^2}{4\sigma_{L\perp}^2}. \end{aligned} \quad (33)$$

In a head-on geometry, this expression reduces to

$$\Sigma_{\theta_L=\pi} = \frac{\sigma_e^2}{4\sigma_{L\parallel}^2} + \frac{\sigma_e^2}{4\sigma_{L\perp}^2}. \quad (34)$$

By expanding Eq. (33) around $\theta_L = 0$ and assuming that $\sigma_{L\perp} \ll \sigma_{L\parallel}$, we find that

$$\Sigma_{\theta_L \ll 1} \simeq \frac{\sigma_e^2}{4\sigma_{L\perp}^2} + \frac{\sigma_z^2}{\sigma_{L\parallel}^2} \gamma^4 \theta_L^2 \quad (35)$$

The important result here is that the electron pulse length, σ_z , starts to have a significant influence on the total x-ray flux compared to the head-on case. Note that $\gamma\theta_L \gg 1$, even in a grazing angle geometry (See Eq. (4)).

Besides the well known bandwidth contribution of the electron angular spread due to the spread in emission angle, $\sigma_\omega/\omega_x|_{\sigma_{\theta_e}} = \gamma^2 \sigma_{\theta_e}^2$, in a grazing angle geometry we also have to take into account that the electron angular spread changes the interaction angle. This creates an x-ray bandwidth contribution

$$\Delta\omega/\omega|_{\sigma_{\theta_e}} = \frac{\beta \sin \theta_L}{1 - \beta \cos \theta_L} \sigma_{\theta_e} \simeq \sqrt{\frac{\omega_x}{\omega_L}} 2\gamma \sigma_{\theta_e}. \quad (36)$$

The approximation on the right holds for $\theta_L \ll 1$.

Finally, we must take into account the effect of the interaction length, $\gamma\beta c\tau_{\text{int}}$, becoming longer than the electron beta function, $\hat{\beta} = \epsilon_n/(\gamma\sigma_{\theta_e}^2)$. In this regime the x-ray source size varies during the interaction and we

can no longer use the electron beam size in the focus as the x-ray source size. Instead we have to use the effective x-ray source size, obtained by a laser intensity-weighted average of the electron beam size:

$$\sigma_{e,\text{eff}}^2 = \sigma_e^2 \left[1 + \frac{1}{2} (\gamma^2 \sigma_{\theta_e}^2 c\tau_{\text{int}}/\epsilon_n)^2 \right]. \quad (37)$$

Equation (37) should be substituted in Eq. (20). It is not required to apply the substitution in Eq. (33) since we will find that in the above mentioned regime, the electron beam becomes very small compared to the laser focus.

D. Optimization of a grazing angle interaction geometry

All ingredients which are required for optimizing the grazing angle interaction geometry are now in place. To arrive at closed form analytic expressions, we first consider the interaction of a single electron with a focused laser pulse and optimize the peak normalized spectral angular density. Next we add the contributions for a realistic electron beam to calculate the corresponding x-ray brilliance. As a final step, we investigate the behavior for small interaction angles $\theta_L \ll 1$, to find the optimized electron energy. This method yields analytical expressions for the laser pulse dimensions, interaction angles, and electron energy for a desired x-ray energy.

For the interaction of a single electron, we optimize the peak normalized spectral angular density given by Eq. (31), to find optimized values of $\sigma_{L\parallel}$ and $\sigma_{L\perp}$. The dependency on the laser pulse dimensions is implicit in A_0 and ζ , given by Eqs. (21) and (23) respectively. We now consider a line focused geometry such that ψ is given by Eq. (27), and recognize that $A_0^2 \propto 1/\sigma_{L\parallel}\sigma_{L\perp}$. We now find that the peak normalized spectral angular density scales as

$$\begin{aligned} \omega_x \mathcal{S}(\omega_x, 0) & \propto \psi^{3/2} h(\psi) \zeta^{3/2} / \sigma_{L\parallel} \\ \text{with } h(\psi) & = \frac{\mathcal{K}_0(\psi^2/4)^2}{\sqrt{1 + \mathcal{K}_0(\psi^2/4)^2}}. \end{aligned} \quad (38)$$

The optimized $\sigma_{L\parallel}$ is found by maximizing $\zeta^{3/2}/\sigma_{L\parallel}$, which occurs when

$$\sigma_{L\parallel}^{\text{opt}} = \frac{1}{\sqrt{2}} \frac{\sin \theta_L}{1 - \beta \cos \theta_L} \beta c \sigma_t. \quad (39)$$

Under this condition, $\zeta = \sqrt{1/3}$. Next, to find the optimized $\sigma_{L\perp}$, we optimize $\psi^{3/2} h(\psi)$, which has a maximum at $\psi_{\text{max}} = 1.91$. When taking into account additional bandwidth contributions such as the electron energy spread, resulting additional terms in the denominator of $h(\psi)$. This will have the effect of decreasing ψ_{max} .

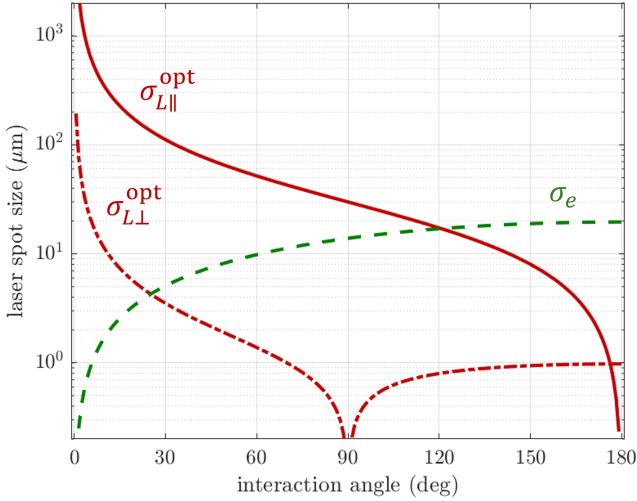


FIG. 8. Optimized laser spot sizes $\sigma_{L\parallel}^{\text{opt}}$ and $\sigma_{L\perp}^{\text{opt}}$ (red solid and dash-dotted curves) and electron spot size σ_e (green dashed curve) for the generation of 500 eV x-rays as a function of interaction angle.

Substituting $\zeta = \sqrt{1/3}$ and $\psi = \psi_{\text{max}}$ into Eq. (27), we also find an expression for the optimized $\sigma_{L\perp}$:

$$\sigma_{L\perp}^{\text{opt}} = \frac{1}{2} \sqrt{\frac{c\sigma_t}{k_L} \left| \frac{\beta \cos \theta_L}{1 - \beta \cos \theta_L} \right| \sqrt{\frac{1}{3} \psi_{\text{max}}}}. \quad (40)$$

The absolute value signs are required since the argument becomes negative when $\theta_L > 90^\circ$.

The red curves in Fig. 8 show the optimized laser spot sizes $\sigma_{L\parallel}$ and $\sigma_{L\perp}$ for the generation of 500 eV x-rays under different interaction angles, according to Eqs. (39) and (40). The figure shows that for small interaction angles the optimal laser spot size σ_L becomes large in both directions; however, the line focus is still maintained: $\sigma_{L\parallel} \gg \sigma_{L\perp}$ over the entire angular range. The green dashed curve shows σ_e for $\epsilon_n = 200$ nrad and $\sigma_\theta = 1$ mrad. Since the optimized laser spot size can become very small outside of the grazing angle geometry, σ_e should always be used as a lower bound for σ_L .

The x-ray brilliance can be calculated by including the effects of the finite electron beam and effective spot size into Eq. (20), resulting in

$$B_x = \frac{fN_e}{2\pi\sigma_e^2(1 + \kappa^2/2)} \frac{1}{1 + \Sigma} \omega_x \mathcal{S}(\omega_x, 0). \quad (41)$$

Here, we have introduced $\kappa = \gamma^2 \sigma_{\theta_e}^2 c \tau_{\text{int}} / \epsilon_n$ which corrects for the effective spot size over the interaction length. For arbitrary interaction angles and beam dimensions the parameters ζ, ψ and Σ should be calculated using Eqs. (23), (25) and (33), respectively. However, in the optimized grazing angle geometry, $\zeta = \sqrt{1/3}$, $\psi = 1.91$,

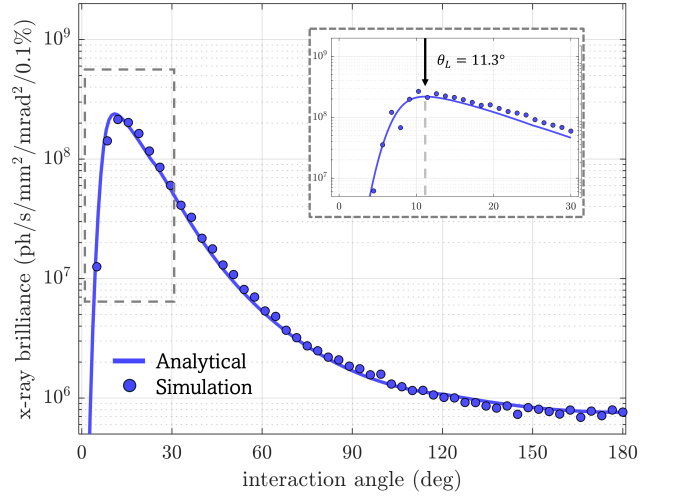


FIG. 9. X-ray brilliance as a function of interaction angle for the generation of 500 eV x-rays, using optimized laser spot sizes $\sigma_{L\parallel}^{\text{opt}}$ and $\sigma_{L\perp}^{\text{opt}}$. The inset zooms in on the $0^\circ - 30^\circ$ angular range, where the arrow denotes the interaction angle corresponding to the optimized electron energy γ_{opt}

and Σ becomes

$$\Sigma = \frac{\sigma_z^2}{6\beta^2 c^2 \sigma_t^2}. \quad (42)$$

In Fig. 9 x-ray brilliance for the generation of 500 eV x-rays is plotted as a function of interaction angle. While the interaction angle is varied, the laser pulse dimensions are also changed, according to Eqs. (39) and (40). The normalized emittance of the electron beam is $\epsilon_n = 200$ nrad and the electron beam angular spread $\sigma_\theta = 1$ mrad. The electron energy is determined by the interaction angle and the fixed x-ray energy of 500 eV. Here σ_e is used as a lower bound for $\sigma_{L\parallel}$ and $\sigma_{L\perp}$.

The figure clearly shows how brilliance increases with decreasing interaction angles, but only up to a point. At small interaction angles, the effective source size becomes so large that the brilliance drops abruptly. This results in an optimal interaction angle, or equivalent electron energy. To find an expression for this optimized electron energy, we analyze how $\sigma_{L\parallel}^{\text{opt}}$ and $\sigma_{L\perp}^{\text{opt}}$ scale for large electron energy. By series expansion of Eq. (2) for $\theta_L \ll 1$ we find that

$$\sigma_{L\parallel}^{\text{opt}} \simeq \sqrt{\frac{\omega_L}{\omega_x}} 2\gamma c \sigma_t, \quad (43)$$

$$\sigma_{L\perp}^{\text{opt}} \simeq \sqrt{\frac{\psi_{\text{max}}}{\omega_x \sigma_t}} \sqrt{\frac{1}{3}} \gamma c \sigma_t. \quad (44)$$

The aspect ratio of the optimized line focus is therefore given by $\sigma_{L\parallel} / \sigma_{L\perp} \simeq 2.15 \sqrt{\omega_L \sigma_t / \psi_{\text{max}}}$. Since the laser spot sizes in both directions become linear with the electron energy, the peak normalized spectral angular density

becomes independent of γ . As a consequence, the x-ray brilliance scales according to

$$B_x \propto \frac{1}{\sigma_{e,\text{eff}}^2} = \frac{\sigma_{\theta_e}^2}{\epsilon_n^2} \frac{\gamma^2}{1 + \kappa^2/2}. \quad (45)$$

Since $\kappa \propto \gamma^3$, we can find the electron energy, γ_{opt} , that optimizes the x-ray brilliance:

$$\gamma_{\text{opt}} = \left[\frac{\omega_L \sigma_{\theta_e}^2}{\omega_x \epsilon_n} 4c\sigma_t \zeta \psi \mathcal{K}_0(\psi^2/4) \right]^{-1/3}. \quad (46)$$

Combining Eq. (46) with Eq. (2) the corresponding interaction angle is obtained. As an example for the parameters used in Fig. 9, the optimized electron energy $\gamma = 103$ and the corresponding optimized interaction angle $\theta_L = 11.3^\circ$. This is in good agreement with the result shown in Fig. 9.

Finally, Eqs. (39) and (40) can be used to find the optimized laser pulse dimensions, completing the full characterization of the optimized grazing angle interaction geometry.

E. Performance of a grazing angle soft x-ray Compton source

As an example, we apply the theoretical framework described above to the design of a soft x-ray Compton source with continuous tunability between 0.25 keV and 2.0 keV. This energy range is highly relevant for life sciences [40, 41] and catalysis [42, 43]. In this energy range, achromatic reflective x-ray optics with focal lengths less than 1 m are available [44], which could keep the footprint within the scale of a university lab.

The electron beamline is based on a high repetition rate C-band photoinjector [30, 31]. This injector creates $Q = 200$ pC electron bunches with a normalized emittance of $\epsilon_n = 200$ nmrad ($\eta = 14$ nmrad/ $\sqrt{\text{pC}}$) and 0.2% energy spread at a repetition rate of $f = 1$ kHz. Subsequent LINACs can be used to accelerate the electrons to the required energy. The electrons are focussed to the interaction point with an angular spread of $\sigma_{\theta_e} = 1$ mrad. The interaction laser is a 100 fs, 5mJ, Yb-fiber system with a central wavelength $\lambda_L = 2\pi c/\omega_L = 1030$ nm, also operating at 1 kHz repetition rate [32]. We assume the electron pulse length to be equal to the laser pulse length.

We compare the x-ray source performance for three geometries. First, a full optimization as described in the previous section is performed, where the electron energy, the interaction angle, and the laser pulse shape are optimized. Second, an optimization is performed in which the electron energy is kept constant and only the interaction angle and the laser pulse shape are optimized. This has the advantage that no re-alignment

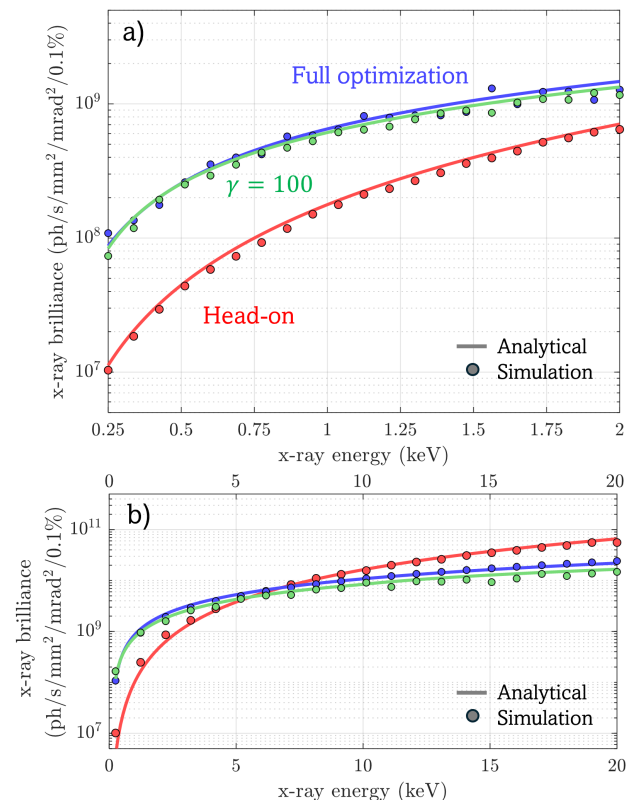


FIG. 10. X-ray brilliance as a function of x-ray energy for three different optimized geometries: head-on scattering (red); grazing angle scattering with optimization of both the interaction angle and the electron energy (blue); and grazing angle scattering with the electron energy kept fixed at $\gamma = 100$ (green). (a) Results for soft x-rays in the range 0.25-2 keV and (b) for the entire range of 0-20 keV.

of the electron optics is required, while the x-ray performance is hardly affected. Finally, a head-on geometry is optimized as described in Sec. II. The resulting analytically optimized x-ray brilliances in the three different geometries are plotted with solid curves in Fig. 10a for the 0.25 – 2 keV soft x-ray energy range and in Fig. 10b for the entire 0 – 20 keV x-ray energy range. Also shown are the results of charged particle tracking simulations (General Particle Tracer [33]) combined with the numerical calculation of the Liénard-Wiechert potentials [34], which are indicated by dots. The analytical model results are in excellent agreement with the numerical calculations.

We find that the grazing angle geometry is able to improve the brilliance of an ICS source in the soft x-ray regime by almost an order of magnitude, compared to the head-on geometry. In addition, we find that the optimization of the grazing angle geometry is hardly affected if the electron energy is not optimized and kept fixed at $\gamma = 100$. Figure 10b shows that the

optimized head-on geometry outperforms the grazing angle geometry only at x-ray energies exceeding 7 keV for the parameters considered.

The performance of the grazing angle geometry could be improved even further by using an appropriate pulse front tilt such that $\zeta \rightarrow 1$. In this case, the x-ray brilliance would increase by approximately the aspect ratio of the laser pulse focus $\sigma_{L\parallel}/\sigma_{L\perp} \simeq 2.15\sqrt{\omega_L\sigma_t/\psi_{\max}}$.

Additionally, the performance of the head-on geometry can be increased by using an appropriately chirped laser pulse to eliminate the effect of nonlinear broadening, which would reduce $\chi \rightarrow 0$.

IV. CONCLUSION

In this paper, we have presented a theoretical approach to optimize inverse Compton scattering x-ray sources. We have found closed form analytical expressions to describe the x-ray beam properties in terms of the laser and electron beam parameters. We find that the interaction angle is an important optimization parameter, which has not yet been treated in great detail. The model not only provides physical intuition on the important scaling of parameters involved in Compton scattering x-ray generation, but also allows for analytical optimization, which is usually done by time consuming simulations. The presented method can serve as a tool for the design of future Compton scattering x-ray sources and the optimization of existing inverse Compton scattering beamlines.

We find that, apart from the conventional head-on interaction geometry, a co-propagating grazing angle interaction can be particularly effective for generating soft x-rays. In general, the optimization involves a subtle interplay between several beam parameters. For a head-on geometry we find the surprising result that lowering the bunch charge can lead to a higher x-ray brilliance while maintaining the same x-ray flux. For soft x-ray wavelengths, optimization of a co-propagating

grazing angle geometry results in an order of magnitude higher x-ray brilliance, compared to the optimized head-on geometry.

Even higher x-ray brilliance could be achieved in a head-on geometry by using chirped laser pulses to suppress the nonlinear broadening. The grazing angle geometry could be optimized even further by employing a laser pulse front tilt, which increases the interaction time without loss of intensity.

ACKNOWLEDGMENTS

We thank Brian Schaap for various fruitful discussions. This research was funded by EU Interreg Vlaanderen-Nederland (Smart*Light project 2.0), by the Ministry of Economic Affairs in the Netherlands through a TKI-grant, and by the Dutch Research Council (NWO) in The Netherlands, through the Industrial Partnership Program (IPP) grant 'ColdLight: From laser-cooled atoms to coherent soft X-rays'.

Appendix A: Derivation of the proper interaction time

We describe ICS in the framework of covariant electrodynamics, when electron recoil can be ignored ($\hbar\omega_x/\gamma m_e c^2 \ll 1$), by assuming an electron with normalized 4-velocity u^μ and 4-trajectory x^μ , interacting with a laser pulse described by the normalized vector potential

$$A^\mu(\tau) = A_0 \exp(-\tau^2/2\tau_{\text{int}}^2) \exp[i\phi(\tau)]\epsilon^\mu, \quad (\text{A1})$$

with $\phi(\tau) = k_L^\nu x_\nu(\tau)$ the laser phase and ϵ^μ is the laser 4-polarization. It is important to note that A^μ describes the vector potential as experienced by the electron, i.e. evaluated at the position and time described by the electron trajectory x^μ . To arrive at Eq. (22) we assume that the amplitude vector potential remains small ($A_0 \ll 1$) and that the laser pulse envelope varies slowly compared to the laser phase. Additionally, we assume that the laser polarization is perpendicular to the initial electron 4-velocity u_0^μ . The spectral angular density of the radiated field is given by [21]

$$\mathcal{S}(\omega, \theta_x) = \frac{\alpha A_0^2}{8\pi} \omega \tau_{\text{int}}^2 \exp\left[-\gamma^2 \tau_{\text{int}}^2 (1 - \beta \cos \theta_x)^2 \left(\omega - \omega_L \frac{1 - \beta \cos \theta_L}{1 - \beta \cos \theta_x}\right)^2\right] \left[1 - \left(\frac{\sin \theta_x \sin \varphi_x}{\gamma(1 - \beta \cos \theta_x)}\right)^2\right], \quad (\text{A2})$$

with φ_x the polar angle of the emitted radiation. In the exponent we can directly identify the angular dependent Doppler shift of Eq. (2) and the Fourier limited bandwidth $\sigma_\omega/\omega_x = [\sqrt{2}\gamma(1 - \beta \cos \theta_L)\omega_L\tau_{\text{int}}]^{-1}$. Evaluation of Eq. (A2) at $\omega = \omega_x$ and $\theta_x = 0$ results in Eq. (22). By

integration over the x-ray frequency we find the angular

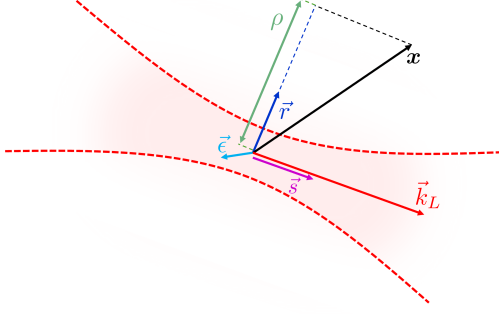


FIG. 11. Illustration of the spatial parts of k_L^μ , r^μ , ϵ^μ and s^μ . The red curve represents the envelope of a Gaussian laser pulse.

radiation distribution

$$\frac{\partial N_x}{\partial \Omega} = \frac{\alpha A_0^2}{8\sqrt{\pi}} \frac{\omega_x \tau_{\text{int}}}{1 - \beta \cos \theta_x} \left[1 - \left(\frac{\sin \theta_x \sin \varphi_x}{\gamma(1 - \beta \cos \theta_x)} \right)^2 \right], \quad (\text{A3})$$

from which we can derive the characteristic $1/\gamma$ cone. When $u_0^\nu \epsilon_\nu \neq 0$, this distribution changes. However, if $\gamma \theta_L \gg 1$ this amounts to a rotation along φ_x .

To find the proper interaction time τ_{int} we must describe the 3D laser pulse in Lorentz invariant quantities. For this we must introduce the following 4-vectors and corresponding invariant contractions:

$$\begin{aligned} \phi &= x_\nu k_L^\nu & k_L^\mu &= k(1, \hat{\mathbf{n}}) \\ \rho &= x_\nu r^\nu & r^\mu &= (0, \hat{\mathbf{e}} \times \hat{\mathbf{n}}) \\ \eta &= x_\nu \epsilon^\nu & \epsilon^\mu &= (0, \hat{\mathbf{e}}) \\ \varsigma &= x_\nu s^\nu & s^\mu &= (0, \hat{\mathbf{n}}) \end{aligned}$$

Figure 11 illustrates how the spatial components of these 4-vectors relate to the laser pulse. We note that, while r^μ and s^μ can be constructed in any reference frame, different observers may not construct the same 4-vectors. These vectors should therefore be interpreted as a tool to describe a laser pulse, rather than manifestly covariant 4-vectors.

We can now describe the vector potential as

$$A^\mu = A_0 \exp \left[-\frac{\rho(\tau)^2}{4\sigma_{L\parallel}^2} - \frac{\eta(\tau)^2}{4\sigma_{L\perp}^2} - \frac{\phi(\tau)^2}{4\omega_L^2 \sigma_t^2} \right] \times \exp [i\phi(\tau)] \epsilon^\mu. \quad (\text{A4})$$

We now assume that the electron has a ballistic trajectory, $x^\mu \simeq u_0^\mu c\tau$, where defined that $x_0^\mu = 0$. This allows the vector potential to be rewritten as

$$A^\mu = A_0 \exp \left(- \left[\frac{(u_0^\nu r_\nu)^2}{4\sigma_{L\parallel}^2} + \frac{(u_0^\nu k_{L\nu})^2}{4\omega_L^2 \sigma_t^2} \right] c^2 \tau^2 \right) \times \exp [i\phi(\tau)] \epsilon^\mu. \quad (\text{A5})$$

Using $u_0^\nu r_\nu = \gamma\beta \sin \theta_L$ and $u_0^\nu k_{L\nu} = \gamma k_L(1 - \beta \cos \theta_L)$ the expression for the proper interaction time (Eq. (24)) can be identified. To incorporate the finite electron beam waist, we take $x_0^\mu = (0, x_0, y_0, z_0)$ and integrate over the electron distribution.

Equation (A5) does not describe a true Gaussian TEM₀₀ mode. Importantly it lacks a description of the divergence, which can be corrected for using the substitution

$$A^\mu \rightarrow A^\mu / \sqrt{1 + (\varsigma/z_R)^2}. \quad (\text{A6})$$

Using $\varsigma = u_0^\nu s_\nu c\tau = \gamma\beta \cos \theta_L c\tau$ we can identify the standard integral

$$\int d\tau \frac{\exp(-\tau^2/2\tau_{\text{int}}^2)}{\sqrt{1 + \tau^2/\tau_R^2}} = \tau_{\text{int}} \psi \exp(\psi^2/4) K_0(\psi^2/4), \quad (\text{A7})$$

with $\psi = \tau_R/\tau_{\text{int}}$. Comparing this to the Gaussian standard integral results in Eq. (26).

Appendix B: Comparison with simulations

Throughout this paper, the developed theory has been checked with simulations. This is done by numerically calculating the spectral angular density from the electron motion with Liénard-Wiechert potentials using the algorithm developed in [34]. The electron motion is calculated using a particle tracking simulation (General Particle Tracer [33]) and the electro-magnetic field descriptions of a pulsed Gaussian TEM₀₀ mode with a focus that can be asymmetrical.

This simulation not only takes into account a more accurate field description, that includes the radius of curvature, Gouy phase, and a diverging laser pulse, it also includes nonlinear effects and ponderomotive scattering. The electron beam is represented by 10^3 macroparticles, where the effects of electron energy spread, divergence and beam size are incorporated. Since the dimensions of the electron beam are much larger than the radiated wavelength, the contributions from individual macroparticles have been added incoherently.

Appendix C: Definition of x-ray brilliance

Throughout this paper we define the x-ray brilliance such that

$$\int B_x \partial A \partial \Omega \partial(\omega/\omega_x) = f N_x, \quad (\text{C1})$$

according to the convention used in [22]. Note that, using this convention, B_x is independent on whether r.m.s., FWHM or other values are used to the define

the quantities ΔA , $\Delta\Omega$ and $\Delta\omega/\omega_x$, as long as a proper normalization is used. Additionally, this definition of x-ray brilliance ensures that Eq. 20 holds. Since σ_e

and $\Delta\omega/\omega_x$ refer to r.m.s. quantities, $\Delta A = 2\pi\sigma_e^2$ and $\Delta\omega/\omega_x = \sqrt{2\pi}\sigma_\omega/\omega_x$. Because the x-ray angular spread is uniform, $\Delta\Omega = \pi\Theta_x^2$. Combining these expressions results in Eq. (1).

-
- [1] P. Sedigh Rahimabadi, M. Khodaei, and K. R. Koswattage, Review on applications of synchrotron-based x-ray techniques in materials characterization, *X-Ray Spectrom.* **49**, 348 (2020).
- [2] W. Thomlinson, H. Elleaume, L. Porra, and P. Suortti, K-edge subtraction synchrotron x-ray imaging in biomedical research, *Phys. Med.* **49**, 58 (2018).
- [3] L. Quenot, S. Bohic, and E. Brun, X-ray phase contrast imaging from synchrotron to conventional sources: A review of the existing techniques for biological applications, *Appl. Sci.* **12**, 9539 (2022).
- [4] M.-E. Couprie, New generation of light sources: Present and future, *J. Electron. Spectrosc. Relat. Phenom.* **196**, 3 (2014).
- [5] B. Günther, R. Gradl, C. Jud, E. Eggl, J. Huang, S. Kulpe, K. Achterhold, B. Gleich, M. Dierolf, and F. Pfeiffer, The versatile x-ray beamline of the munich compact light source: design, instrumentation and applications, *J. Synchrotron Radiat.* **27**, 1395 (2020).
- [6] Y. Du, L. Yan, J. Hua, Q. Du, Z. Zhang, R. Li, H. Qian, W. Huang, H. Chen, and C. Tang, Generation of first hard x-ray pulse at tsinghua thomson scattering x-ray source, *Rev. Sci. Instrum.* **84** (2013).
- [7] M. Alkadi, M. Alves, M. Amer, L. Amoudry, D. Auguste, J.-L. Babigeon, M. Baltazar, A. Benoit, A. Blin, M. Bonanzingamarco, *et al.*, Commissioning of thomx compton source subsystems and demonstration of 10^{10} x-rays/s, *Phys. Rev. Accel. Beams* **28**, 023401 (2025).
- [8] W. Graves, J. Bessuille, P. Brown, S. Carbajo, V. Dolgashev, K.-H. Hong, E. Ihloff, B. Khaykovich, H. Lin, K. Murari, *et al.*, Compact x-ray source based on burst-mode inverse compton scattering at 100 khz, *Phys. Rev. ST Accel. Beams* **17**, 120701 (2014).
- [9] I. J. M. V. Elk, C. W. Sweers, D. F. J. Nijhof, R. G. W. V. den Berg, T. G. Lucas, X. F. D. Stragier, P. Tack, M. N. Boone, O. J. Luiten, and P. H. A. Mutsaers, First x-rays from a compact and tunable linac-based compton scattering source, *Opt. Express* **33**, 47498 (2025).
- [10] C. P. Barty, J. M. Algots, A. J. Amador, J. C. Barty, S. M. Betts, M. A. Castañeda, M. M. Chu, M. E. Daley, R. A. De Luna Lopez, D. A. Diviak, *et al.*, Design, construction, and test of compact, distributed-charge, x-band accelerator systems that enable image-guided, vhee flash radiotherapy, *Front. Phys.* **12**, 1472759 (2024).
- [11] L. Amoudry, M. Kravchenko, R. Berry, N. Burger, A. Diego, J. Edelen, M. Ruelas, R. Agustsson, G. Andonian, Y.-C. Chen, *et al.*, Commissioning of a photocathode and interaction laser system at radiabeam compact inverse compton light source, *Nucl. Instrum. Methods Phys. Res. A: Accel. Spectrom. Detect. Assoc. Equip* **1075**, 170287 (2025).
- [12] L. Faillace, R. G. Agostino, A. Bacci, R. Barberi, A. Bosotti, F. Broggi, P. Cardarelli, S. Cialdi, I. Drebot, V. Formoso, *et al.*, Status of compact inverse compton sources in italy: Brixs and star, in *Advances in Laboratory-based X-Ray Sources, Optics, and Applications VII*, Vol. 11110 (SPIE, 2019) pp. 14–21.
- [13] T. Brümmer, S. Bohlen, F. Grüner, J. Osterhoff, and K. Pöder, Compact all-optical precision-tunable narrow-band hard compton x-ray source, *Sci. Rep.* **12**, 16017 (2022).
- [14] V. Musat, P. Burrows, S. Doebert, E. Granados, J. Herador, A. Latina, and A. Malyzhenkov, A compact water window x-ray source based on inverse compton scattering (JACoW Publishing, 2024) pp. 441–444.
- [15] B. Schaap, A. Murokh, and P. Musumeci, An inverse free electron laser-bunching driven shallow-angle superradiant compton source, *Nucl. Instrum. Methods Phys. Res. A: Accel. Spectrom. Detect. Assoc. Equip* **1066**, 169576 (2024).
- [16] B. Günther, I. Kokhanovskyi, M. Dierolf, K. Achterhold, and F. Pfeiffer, Rapid x-ray energy switching for optimised k-edge subtraction imaging at narrow-band inverse compton x-ray sources, *Opt. Express* **33**, 47321 (2025).
- [17] D. Berthe, L. Heck, S. Resch, M. Dierolf, J. Brantl, B. Günther, C. Petrich, K. Achterhold, F. Pfeiffer, S. Grandl, K. Hellerhoff, and J. Herzen, Grating-based phase-contrast computed tomography for breast tissue at an inverse compton source, *Sci. Rep.* **14**, 10.1038/s41598-024-77346-1 (2024).
- [18] D. J. Batey, F. Van Assche, S. Vanheule, M. N. Boone, A. J. Parnell, O. O. Mykhaylyk, C. Rau, and S. Cipiccia, X-ray ptychography with a laboratory source, *Phys. Rev. Lett.* **126**, 193902 (2021).
- [19] F. V. Hartemann and S. S. Wu, Nonlinear brightness optimization in compton scattering, *Phys. Rev. Lett.* **111**, 044801 (2013).
- [20] E. Esarey, S. K. Ride, and P. Sprangle, Nonlinear thomson scattering of intense laser pulses from beams and plasmas, *Phys. Rev. E* **48**, 3003 (1993).
- [21] B. H. Schaap, T. De Vos, P. Smorenburg, and O. J. Luiten, Photon yield of superradiant inverse compton scattering from microbunched electrons, *New J. Phys.* **24**, 033040 (2022).
- [22] D. Attwood, *Soft x-rays and extreme ultraviolet radiation: principles and applications* (Cambridge university press, 2000).
- [23] J. D. Jackson, *Classical electrodynamics*, 2nd ed. (Wiley, New York, NY, 1975).
- [24] M. Furman, The moller luminosity factor (Lawrence Berkeley National Laboratory, 2003).
- [25] V. Petrillo, A. Bacci, R. B. A. Zinati, I. Chaikovska, C. Curatolo, M. Ferrario, C. Maroli, C. Ronsivalle, A. Rossi, L. Serafini, *et al.*, Photon flux and spectrum of γ -rays compton sources, *Nucl. Instrum. Methods Phys. Res. A: Accel. Spectrom. Detect. Assoc. Equip* **693**, 109 (2012).
- [26] M. Abramowitz and I. A. Stegun, *Handbook of mathematical functions with formulas, graphs, and mathematical tables*, Vol. 55 (US Government printing office, 1948).

- [27] F. V. Hartemann, F. Albert, C. W. Siders, and C. Barty, Low-intensity nonlinear spectral effects in Compton scattering, *Phys. Rev. Lett.* **105**, 130801 (2010).
- [28] B. Terzić, J. McKaig, E. Johnson, T. Dharanikota, and G. A. Krafft, Laser chirping in inverse Compton sources at high electron beam energies and high laser intensities, *Phys. Rev. Accel. Beams* **24**, 094401 (2021).
- [29] P. Pasmans, D. Van Vugt, J. Van Lieshout, G. Brussaard, and O. Luiten, Extreme regimes of femtosecond photoemission from a copper cathode in a dc electron gun, *Phys. Rev. Accel. Beams* **19**, 103403 (2016).
- [30] T. G. Lucas, H.-H. Braun, P. Craievich, R. Fortunati, N. Kirchgeorg, A. Magazinik, M. Pedrozzi, J.-Y. Raguin, S. Reiche, M. Schaer, *et al.*, Toward a brightness upgrade to the SwissFEL: A high gradient traveling-wave rf photogun, *Phys. Rev. Accel. Beams* **26**, 103401 (2023).
- [31] D. Alesini, F. Cardelli, G. Di Raddo, L. Faillace, M. Ferrario, A. Gallo, A. Giribono, G. Latini, S. Lauciani, A. Liedl, *et al.*, Design, realization, and testing of a brazing-free c-band radio frequency photogun, *Phys. Rev. Accel. Beams* **29**, 012001 (2026).
- [32] *PHAROS, Modular-Design Femtosecond Lasers for Industry and Science*, Light Conversion (2025).
- [33] Pulsar Physics, General Particle Tracer (GPT), General Particle Tracer (GPT), <http://www.pulsar.nl/gpt>.
- [34] A. Thomas, Algorithm for calculating spectral intensity due to charged particles in arbitrary motion, *Phys. Rev. ST Accel. Beams* **13**, 020702 (2010).
- [35] K. Steiniger, M. Bussmann, R. Pausch, T. Cowan, A. Irman, A. Jochmann, R. Sauerbrey, U. Schramm, and A. Debus, Optical free-electron lasers with traveling-wave Thomson-scattering, *J. Phys. B: At. Mol. Opt. Phys.* **47**, 234011 (2014).
- [36] A. Potylitsyn, D. Gavrilenko, M. Strikhanov, and A. Tishchenko, Crab crossing in inverse Compton scattering, *Phys. Rev. Accel. Beams* **26**, 040701 (2023).
- [37] B. Schaap, M. Lenz, and P. Musumeci, Shallow angle inverse Compton scattering, arXiv preprint arXiv:2509.04621 (2025).
- [38] H. Zhang, Y. Du, Z. Chi, L. Yan, W. Huang, and C. Tang, Experimental demonstration of polarization control in Thomson scattering x-ray sources, *Nucl. Instrum. Methods Phys. Res. A: Accel. Spectrom. Detect. Assoc. Equip* **1064**, 169376 (2024).
- [39] B. H. Schaap, C. W. Sweers, P. Smorenburg, and O. Luiten, Ponderomotive bunching of a relativistic electron beam for a superradiant Thomson source, *Phys. Rev. Accel. Beams* **26**, 074401 (2023).
- [40] M. Kördel, A. Dehlinger, C. Seim, U. Vogt, E. Fogelqvist, J. A. Sellberg, H. Stiel, and H. M. Hertz, Laboratory water-window x-ray microscopy, *Optica* **7**, 658 (2020).
- [41] V. Weinhardt and C. Larabell, Soft x-ray tomography has evolved into a powerful tool for revealing cell structures, *Annu. Rev. Anal. Chem.* **18** (2025).
- [42] C. Cao, M. F. Toney, T.-K. Sham, R. Harder, P. R. Shearing, X. Xiao, and J. Wang, Emerging x-ray imaging technologies for energy materials, *Mater. Today* **34**, 132 (2020).
- [43] S. K. Beaumont, Soft xas as an in situ technique for the study of heterogeneous catalysts, *Phys. Chem. Chem. Phys.* **22**, 18747 (2020).
- [44] T. Kimura, Y. Takeo, K. Sakurai, N. Furuya, S. Egawa, G. Yamaguchi, Y. Matsuzawa, T. Kume, H. Mimura, M. Shimura, *et al.*, Soft x-ray ptychography system using a Wolter mirror for achromatic illumination optics, *Opt. Express* **30**, 26220 (2022).